

SELF-CONSISTENT VELOCITY MATCHING OF PROBABILITY FLOWS

Lingxiao Li
MIT CSAIL
lingxiao@mit.edu

Samuel Hurault
Univ. Bordeaux, Bordeaux INP, CNRS, IMB
samuel.hurault@math.u-bordeaux.fr

Justin Solomon
MIT CSAIL
jsolomon@mit.edu

ABSTRACT

We present a discretization-free scalable framework for solving a large class of mass-conserving partial differential equations (PDEs), including the time-dependent Fokker-Planck equation and the Wasserstein gradient flow. The main observation is that the time-varying velocity field of the PDE solution needs to be *self-consistent*: it must satisfy a fixed-point equation involving the flow characterized by the same velocity field. By parameterizing the flow as a time-dependent neural network, we propose an end-to-end iterative optimization framework called *self-consistent velocity matching* to solve this class of PDEs. Compared to existing approaches, our method does not suffer from temporal or spatial discretization, covers a wide range of PDEs, and scales to high dimensions. Experimentally, our method recovers analytical solutions accurately when they are available and achieves comparable or better performance in high dimensions with less training time compared to recent large-scale JKO-based methods that are designed for solving a more restrictive family of PDEs.

1 INTRODUCTION

Mass conservation is a ubiquitous phenomenon in dynamical systems arising from fluid dynamics, electromagnetism, thermodynamics, and stochastic processes. Mathematically, mass conservation is formulated as the *continuity equation*:

$$\partial_t p_t(x) = -\nabla \cdot (v_t p_t), \forall x, t \in [0, T] \quad (1)$$

where $p_t : \mathbf{R}^d \rightarrow \mathbf{R}$ is a scalar quantity such that the total mass $\int p_t(x)$ is conserved with respect to t , $v_t : \mathbf{R}^d \rightarrow \mathbf{R}^d$ is a velocity field, and $T > 0$ is total time. We will assume, for all $t \in [0, T]$, $p_t \geq 0$ and $\int p_t(x) dx = 1$, i.e., p_t is a probability density function. We use μ_t to denote the probability measure with density p_t . Once a pair (p_t, v_t) satisfies (1), the density p_t is coupled with v_t in the sense that the evolution of p_t in time is characterized by v_t (Section 3.1).

We consider the subclass of mass-conserving PDEs that can be written in a single equation of the form

$$\partial_t p_t(x) = -\nabla \cdot (f_t(x; \mu_t) p_t), \forall x, t \in [0, T] \quad (2)$$

where $f_t(\cdot; \mu_t) : \mathbf{R}^d \rightarrow \mathbf{R}^d$ is a given function depending on μ_t , with initial condition $\mu_0 = \mu_0^*$ for a given initial probability measure μ_0^* with density p_0^* .

Different choices of f_t lead to a large class of mass-conserving PDEs. For instance, given a functional $\mathcal{F} : \mathcal{P}_2(\mathbf{R}^d) \rightarrow \mathbf{R}$ on the space of probability distributions with finite second moments, if we take

$$f_t(x; \mu_t) := -\nabla_{W_2} \mathcal{F}(\mu_t)(x), \quad (3)$$

where $\nabla_{W_2} \mathcal{F}(\mu) : \mathbf{R}^d \rightarrow \mathbf{R}^d$ is the Wasserstein gradient of \mathcal{F} , then the solution to (2) is the Wasserstein gradient flow of \mathcal{F} (Santambrogio, 2015, Chapter 8). Thus, solving (2) efficiently

allows us to optimize in the probability measure space. If we take

$$f_t(x; \mu_t) := b_t(x) - D_t(x) \nabla \log p_t(x), \quad (4)$$

where b_t is a velocity field and $D_t(x)$ is a positive-semidefinite matrix, then we obtain the time-dependent Fokker-Planck equation Risken & Risken (1996), which describes the time evolution of the probability flow undergoing drift b_t and diffusion with coefficient D_t .

The predominant strategy to solve (2) is to use an Eulerian representation of the density field p_t on a discretized mesh or as a neural network (Raissi et al., 2019). However, these approaches do not fully exploit the mass-conservation principle and are difficult to scale to high dimensions. Shen et al. (2022) recently introduced the notion of *self-consistency* for the Fokker-Planck equation, a Lagrangian formulation of (2) involving the velocity field of the flow. In this work, we extend their notion of self-consistency to a more general class of mass-conserving PDEs of the form (2). To this end, we develop an iterative optimization scheme called *self-consistent velocity matching*. With the probability flow parameterized as a neural network, at each iteration, we refine the velocity field v_t of the current flow to match an estimate of f_t evaluated using the network weights from the previous iteration. This iterative formulation allows us to rewrite the velocity-matching objectives for certain PDEs to get rid of the computationally expensive quantities such as $\nabla \log p_t$ in the Fokker-Planck equation. Moreover, our method is agnostic to the probability flow parameterization: we have empirically found that the two popular ways of parameterizing the flow—as a time-varying pushforward map (Biloš et al., 2021) and as a time-varying velocity field (Chen et al., 2018)—both have merits in different scenarios.

Our method tackles mass-conserving PDEs of the form (2) in a unified manner without temporal or spatial discretization. Experimentally, it can recover true solutions faithfully for PDEs with analytically-known solutions. Only recent neural JKO-based methods (Mokrov et al., 2021; Fan et al., 2021; Alvarez-Melis et al., 2021) are capable of solving PDEs of the form (2) in high dimensions, and these methods are specialized to Wasserstein gradient flows (3). Our algorithm achieves comparable or better performance in our test cases compared to these JKO methods while using a lower computational budget and without discretizing time. We further demonstrate the flexibility of our method on a series of qualitative experiments for modeling flocks of birds, flows splashing against obstacles, and computing smooth interpolation of measures, all without discretization.

2 RELATED WORKS

Classical PDE solvers for mass-conserving PDEs such as the Fokker-Planck equation and the Wasserstein gradient flow either use an Eulerian representation of the density and discretize space as a grid or mesh Burger et al. (2010); Carrillo et al. (2015); Peyré (2015) or use a Lagrangian representation, which discretizes the flow as a collection of interacting particles simulated forward in time Crisan & Lyons (1999); Westdickenberg & Wilkening (2010). Due to spatial discretization, these methods struggle with high-dimensional problems. Hence, the rest of the section focuses solely on recent neural network-based methods.

Physics-informed neural networks. Physics-informed neural networks (PINNs) are prominent methods that solve PDEs using deep learning (Raissi et al., 2019; Karniadakis et al., 2021). The main idea is to minimize the residual of the PDE along with loss terms to enforce the boundary conditions and to match observed data. Our notion of self-consistency is a Lagrangian analog of the residual in PINN. Our velocity matching only occurs along the flow of the current solution where interesting dynamics happen, while in PINNs the residual is evaluated on collocation points that occupy the entire domain. Hence our method is particularly suitable for high-dimensional problems where the dynamics have a low-dimensional structure.

Neural JKO methods. Recent works (Mokrov et al., 2021; Alvarez-Melis et al., 2021; Fan et al., 2021) apply deep learning to the time-discretized JKO scheme (Jordan et al., 1998) to solve Wasserstein gradient flow (3). By pushing a reference measure through a chain of neural networks, usually parameterized as input-convex neural networks (ICNNs) (Amos et al., 2017), these methods avoid discretizing the space and are thus capable of solving high-dimensional problems. Mokrov et al. (2021) optimize one ICNN to minimize Kullback-Leibler (KL) divergence plus a Wasserstein-2 distance term at each JKO step. This method is extended to other functionals by Alvarez-Melis et al.

(2021). Fan et al. (2021) use the variational formulation of f -divergence to obtain a faster primal-dual approach.

An often overlooked problem of neural JKO methods is that the total training time scales quadratically with the number of JKO steps: to draw samples for the current step, initial samples from the reference measure must be passed through a long chain of neural networks, along with expensive quantities like densities. However, using too few JKO steps results in large temporal discretization errors. Moreover, the optimization at each step might not have fully converged before the next step begins, resulting in an unpredictable accumulation of errors. In contrast, our method does not suffer from temporal discretization and can be trained end-to-end. It outperforms these neural JKO methods with less training time in most experiments we considered.

Velocity matching. A few recent papers employ the idea of velocity matching to construct a flow that follows a learned velocity field. di Langosco et al. (2021) simulate the Wasserstein gradient flow of the KL divergence by learning a velocity field that drives a set of particles forward in time for Bayesian posterior inference. The velocity field is refined on the fly based on the current positions of the particles. Boffi & Vanden-Eijnden (2022) propose a similar method that applies to a more general class of time-dependent Fokker-Planck equations. These two methods can only approximate probability measures using finite particles and can have large temporal discretization errors similar to JKO methods. Two recent methods (Liu et al., 2022; Lipman et al., 2022) use flow matching for generative modeling by learning a velocity field that generates a probability path connecting a reference distribution to the data distribution. Yet these two methods are not designed for solving PDEs.

Most relevant to our work, Shen et al. (2022) propose the concept of self-consistency for the Fokker-Planck equation, that the velocity field recovering the velocity field of the flow solution to the Fokker-Planck equation must satisfy a fixed-point equation. They theoretically show that, under certain regularity conditions, the Wasserstein-2 distance between the current solution and the true solution is bounded by a term measuring the violation of the fixed-point equation (including up to second-order spatial derivatives). Their algorithm minimizes such violation using neural ODE parameterization (Chen et al., 2018) and the adjoint method. Our work extends the concept of self-consistency to a wider class of PDEs in the form of (2). Unlike Shen et al. (2022), our method does not optimize a fixed objective but instead carries out infinite-dimensional fixed-point iterations on the self-consistency condition. While the experiments of Shen et al. (2022) are limited to a simple 2D example, presumably due to the computational cost of the higher-order spatial derivatives in their objective, our method excels at solving a variety of large-scale problems.

3 SELF-CONSISTENT VELOCITY MATCHING

3.1 PROBABILITY FLOW OF THE CONTINUITY EQUATION

A key property of the continuity equation (1) is that any solution $(p_t, v_t)_{t \in [0, T]}$ (provided p_t is continuous with respect to t and v_t is bounded) corresponds to a unique flow map $\{\Phi_t(\cdot) : \mathbf{R}^d \rightarrow \mathbf{R}^d\}_{t \in [0, T]}$ that solves the ordinary differential equations (ODEs) (Ambrosio et al., 2005, Proposition 8.1.8)

$$\Phi_0(x) = x, \frac{d}{dt}\Phi_t(x) = v_t(\Phi_t(x)), \forall x, t \in [0, T], \quad (5)$$

and the flow map satisfies $\mu_t = (\Phi_t)_\# \mu_0$ for all $t \in [0, T]$, where $(\Phi_t)_\# \mu_0$ to denote the push-forward measure of μ_0 by Φ_t . Moreover, the converse is true: any solution (Φ_t, v_t) of (5) with Lipschitz continuous and bounded v_t is a solution of (1) with $\mu_t = (\Phi_t)_\# \mu_0$ (Ambrosio et al., 2005, Lemma 8.1.6). Thus the Eulerian viewpoint of (1) is equivalent to the Lagrangian viewpoint of (5). We next exploit this equivalence by modeling the probability flow using the Lagrangian viewpoint so that it automatically satisfies the continuity equation (1).

3.2 PARAMETRIZING PROBABILITY FLOWS

Our algorithm will be agnostic to the exact parameterization used to represent the probability flow. As such, we need a way to parameterize the flow to access the following quantities for all $t \in [0, T]$:

- $\Phi_t : \mathbf{R}^d \rightarrow \mathbf{R}^d$, the flow map at time t . $\Phi_t(x_0)$ is the location of a particle at time t if it is at x_0 at time 0. We assume Φ_t is invertible;
- $v_t : \mathbf{R}^d \rightarrow \mathbf{R}^d$, the velocity field of the flow at time t .
- $\mu_t \in \mathcal{P}(\mathbf{R}^d)$, the probability measure at time t from which we can access samples and its density p_t .

We will assume all these quantities are sufficiently continuous and bounded to ensure the Eulerian and Lagrangian viewpoints in Section 3.1 are equivalent. This can be achieved by using continuously differentiable activation functions in the network architectures and assuming the network weights are finite similar to the uniqueness arguments given in (Chen et al., 2018). We will use the following two ways to parameterize the flow, modeling either the flow map Φ_t or the velocity field v_t as a neural network.

Time-dependent Invertible Push Forward (TIPF). We first parameterize a probability flow by modeling $\Phi_t : \mathbf{R}^d \rightarrow \mathbf{R}^d$ as an invertible network for every t . The network architecture is chosen so that Φ_t has an analytical inverse with a tractable Jacobian determinant, similar to (Biloš et al., 2021). We augment RealNVP (Dinh et al., 2016) so that the network for predicting scale and translation takes t as an additional input. To enforce the initial condition, we need Φ_0 to be the identity map. This condition can be baked into the network architecture (Biloš et al., 2021) or enforced by adding an additional loss term $\mathbf{E}_{X \sim \mu_0^*} \|\Phi_0(X) - X\|^2$. For brevity, we will from now on omit in the text this additional loss term. The velocity field can be recovered via $v_t(x) = \partial_t \Phi_t(\Phi_t^{-1}(x))$. To recover the density p_t of $\mu_t = (\Phi_t)_\# \mu_0$, we use the change-of-variable formula $\log p_t(x) = \log p_0^*(\Phi_t^{-1}(x)) + \log \det |J\Phi_t^{-1}(x)|$.

Neural ODE (NODE). We also parameterize a flow by modeling $v_t : \mathbf{R}^d \rightarrow \mathbf{R}^d$ as a neural network; this is used in Neural ODE (Chen et al., 2018). The network only needs to satisfy the minimum requirement of being continuous. The flow map and the density can be recovered via numerical integration: $\Phi_t(x) = x + \int_0^t v_s(\Phi_s(x)) ds$ and $\log p_t(\Phi_t(x)) = \log p_0^*(x) - \int_0^t \nabla \cdot v_s(\Phi_s(x)) ds$, a direct consequence of (1) also known as the instantaneous change-of-variable formula (Chen et al., 2018). To obtain the inverse of the flow map, we integrate along $-v_t$. With NODE, the initial condition $\mu_0 = \mu_0^*$ is obtained for free.

While the use of invertible coupling layers in TIPF allows efficient access to samples and densities, TIPF becomes less effective in higher dimensions as many couple layers are needed to retain good expressive power. In contrast, NODE puts little constraints on the network architecture, but numerical integration can be slow and have errors. Handling the initial condition is trivial for NODE while an additional loss term or special architecture is needed for TIPF. As we will show in the experiments, both strategies have merits.

3.3 FORMULATION

We now describe our algorithm for solving mass-conserving PDEs (2). A PDE of this form is determined by $f_t(\cdot; \mu_t) : \mathbf{R}^d \rightarrow \mathbf{R}^d$ plus the initial condition μ_0^* . If a probability flow μ_t with flow map Φ_t and velocity field v_t satisfies the following *self-consistency* condition,

$$v_t(x) = f_t(x; \mu_t), \forall x \text{ in the support of } \mu_t, \quad (6)$$

then the continuity equation of this flow implies the corresponding PDE (2) is solved. Conversely, the velocity field of any solution of (2) will satisfy (6). Shen et al. (2022) develop this concept for the Fokker-Planck equation, and here we generalize it to a wider class of PDEs of the form (2). Hence, instead of solving (2) which is a condition on the density p_t that might be hard to access, we can solve (6) which is a more tractable condition on the velocity field v_t that is readily accessible using TIPF or NODE.

Let θ be the network weights that parameterize the probability flow using TIPF or NODE. The flow's measure, velocity field, and flow map at time t are denoted as $\mu_t^\theta, v_t^\theta, \Phi_t^\theta$ respectively. One option to solve (6) would be to minimize

$$\min_{\theta} \int_0^T \mathbf{E}_{X \sim \mu_t^\theta} \left[\|v_t^\theta(X) - f_t(X; \mu_t^\theta)\|^2 \right] dt. \quad (7)$$

This formulation is reminiscent of PINNs (Raissi et al., 2019) where a residual of the original PDE is minimized. Direct optimization of (7) is challenging: while the integration over $[0, T]$ and μ_t^θ can be

approximated using Monte Carlo, to apply stochastic gradient descent, we must differentiate through the μ_t^θ and f_t : this can be either expensive or intractable depending on the network parameterization. The algorithm by Shen et al. (2022) uses the adjoint method specialized to Fokker-Planck equations; extending their approach to more general PDEs requires a closed-form formula for the time evolution of the quantities within f_t , which can only be obtained on a case-by-case basis.

Instead, we propose the following iterative optimization algorithm to solve (7). Let θ_k denote the network weights at iteration k . We define iterates

$$\theta_{k+1} := \arg \min_{\theta} F(\theta, \theta_k). \quad (8)$$

where

$$F(\theta, \theta_k) := \int_0^T \mathbf{E}_{X \sim \mu_t^{\theta_k}} \left[\left\| v_t^\theta(X) - f_t(X; \mu_t^{\theta_k}) \right\|^2 \right]. \quad (9)$$

Effectively, in (9), we only match the velocity field v_t^θ to what it should be according to f_t based on the network weights θ_k from the previous iteration. This scheme is an infinite-dimensional analog to fixed-point iterations as v_t is a continuous vector field. Since θ_k is fixed, minimizing (9) over θ is a lot easier than directly minimizing (7), as v_t^θ only needs to match a constant velocity field $f_t(\cdot; \mu_t^{\theta_k})$; we found a few steps of stochastic gradient descent sufficient for the optimization in (8) (see a comparison in Figure 13). We call this iterative algorithm *self-consistent velocity matching*.

If f_t depends on the density of μ_t only through the score $\nabla \log p_t$ (corresponding to a diffusion term in the PDE), then we can apply an integration-by-parts trick (Hyvärinen & Dayan, 2005) to get rid of this density dependency by adding a divergence term of the velocity field. Suppose f_t is from the Fokker-Planck equation (4). Then the cross term in (9) after expanding the squared norm has the following alternative expression.

Proposition 3.1. *For every $t \in [0, T]$, for f_t defined in (4), assume v_t^θ, D_t are bounded and continuously differentiable, and $\mu_t^{\theta'}$ is a measure with a continuously differentiable density $p_t^{\theta'}$ that vanishes in infinity and not at finite points, then we have*

$$\begin{aligned} \mathbf{E}_{X \sim \mu_t^{\theta'}} \left[v_t^\theta(X)^\top f_t(X; \mu_t^{\theta'}) \right] = \\ \mathbf{E}_{X \sim \mu_t^{\theta'}} \left[v_t^\theta(X)^\top b_t(X) + \nabla \cdot (D_t^\top(x) v_t^\theta(X)) \right]. \end{aligned} \quad (10)$$

We provide the derivation in Appendix A. Minimizing (9) is then equivalent to minimizing the expectation of the squared norm of v_t^θ plus the cross term (10), and access to p_t is no longer needed. This is useful for NODE parameterization since obtaining the score would otherwise require additional numerical integration.

3.4 PRACTICAL ALGORITHM

We apply stochastic gradient descent to solve (9) using the Adam optimizer (Kingma & Ba, 2014). Our algorithm is summarized in Algorithm 1. For sampling time steps t_1, \dots, t_L in $[0, T]$, we use stratified sampling where t_l is uniformly sampled from $[(l-1)T/L, lT/L]$; such a sampling strategy results in more stable training in our experiments. We retain the optimizer state of Adam from iteration k to iteration $k + 1$.

We implemented our method using JAX (Bradbury et al., 2018) and FLAX (Heek et al., 2020). See Appendix B for the implementation details.

4 EXPERIMENTS

We show the efficiency and accuracy of our method on several PDEs of the form (2). We start with three Wasserstein gradient flow experiments (Section 4.1, Section 4.2, Section 4.3) and compare against JKO methods by Mokrov et al. (2021) and Fan et al. (2021). We will not compare against Alvarez-Melis et al. (2021) since it is the same as JKO-ICNN except with a log det approximation; we will not use such approximation to ensure accurate results. Next, we consider the time-dependent

Algorithm 1 Self-consistent velocity matching

Input: $f_t(\cdot, \cdot)$, μ_0^* , T , N_{train} , N_{inner} , B , L .
Initialize network weights θ .
for $k = 1, \dots, N_{\text{train}}$ **do**
 $\theta' \leftarrow \theta$.
 for $j = 1, \dots, N_{\text{inner}}$ **do**
 Sample $x_1, \dots, x_B \sim \mu_0^*$, $t_1, \dots, t_L \sim [0, T]$.
 $y_{b,l} \leftarrow \Phi_{t_l}^{\theta'}(x_b)$, $\forall b = 1, \dots, B, l = 1, \dots, L$.
 Minimize $\frac{1}{BL} \sum_{b,l} \left\| v_t^\theta(y_{b,l}) - f_t(y_{b,l}; (\Phi_{t_l}^{\theta'})_{\#} \mu_0^*) \right\|^2$ over θ for one gradient step.
 end for
end for
Output: optimized θ .

Fokker-Planck equation in Section 4.4 and compare it against the Euler-Maruyama method for simulating stochastic differential equations (Higham, 2001). Finally, in Section 4.5 we show that our framework is capable of generating complicated dynamics in dimension 2. We will use SCVM-TIPF and SCVM-NODE to denote our method with TIPF and NODE parameterization respectively. We use JKO-ICNN to denote the method by Mokrov et al. (2021) and JKO-ICNN-PD to denote the method by Fan et al. (2021) (PD for “primal-dual”). We use SDE-EM to denote the Euler-Maruyama method. We implemented all competing methods in JAX—see more details in Appendix B. For JKO methods, we always use 40 JKO steps.

Evaluation metrics. For quantitative evaluation, we use the following metrics. To compare measures with density access, following Mokrov et al. (2021), we use the symmetric Kullback-Leibler (symmetric KL) divergence, defined as $\text{SymKL}(\rho_1, \rho_2) := \text{KL}(\rho_1 \parallel \rho_2) + \text{KL}(\rho_2 \parallel \rho_1)$, where $\text{KL}(\rho_1 \parallel \rho_2) := \mathbf{E}_{X \sim \rho_1}[\log \frac{d\rho_1(X)}{d\rho_2(X)}]$. When estimating symmetric KL divergence using samples, due to the finite sample size and the numerical error in estimating the log density, the estimated divergence can be negative when it is close to zero—when this occurs we take absolute values. We also consider an alternative f -divergence $D_f(\rho_1 \parallel \rho_2) := \mathbf{E}_{X \sim \rho_2}[(\log \rho_1(X) - \log \rho_2(X))^2/2]$. Compared to KL divergence, sample estimates of D_f are always positive. We similarly define the symmetric f -divergence $\text{Sym}D_f(\rho_1, \rho_2) := D_f(\rho_1 \parallel \rho_2) + D_f(\rho_2 \parallel \rho_1)$. To compare measures with only sample access, we consider the energy distance (Székely & Rizzo, 2013) and the Wasserstein-2 distance (Bonneel et al., 2011). More details on the metric calculations are given in Appendix B.4.

4.1 SAMPLING FROM MIXTURES OF GAUSSIANS

We consider computing the Wasserstein gradient flow of the KL divergence $\mathcal{F}(\mu) = \text{KL}(\mu \parallel \mu^*)$ where we have density access to the target measure μ^* . To fit into our framework, we set $f_t(x; \mu_t) = \nabla \log p^*(x) - \nabla \log p_t(x)$ which matches (4) with $b_t(x) = \nabla \log p^*(x)$ and $D_t(x) = I_d$. Following the experimental setup in Mokrov et al. (2021) and Fan et al. (2021), we take μ^* to be a mixture of 10 Gaussians with identity covariance and means sampled uniformed in $[-5, 5]^d$. The initial measure is $\mu_0^* = \mathcal{N}(0, 16I_d)$. We solve the corresponding Fokker-Planck PDE for a total time of $T = 5$ and for $d = 10, \dots, 60$. As TIPF parameterization does not scale to high dimensions, we only consider SCVM-NODE in this experiment.

Figure 1 shows the samples produced by SCVM-NODE align well with those from the target measure in dimension 60 at $t = T$. In Figure 14, we visualize μ_t produced by our method at irregular time steps.

We quantitatively compare our solutions with those from Mokrov et al. (2021) and Fan et al. (2021). In Figure 2, we plot various metrics for all methods at $t = 5$ (compared against the target distribution) while varying the dimension d . The running time of Mokrov et al. (2021) becomes prohibitively long (5 hours for $d = 30$), so we only include its result for $d \leq 30$. In Figure 3, we plot the same metrics as functions of t for $d = 30$ and $d = 60$. We see that SCVM-NODE achieves far lower metrics in all dimensions considered. We notice the gradient flow computed by JKO methods might not result in monotonically decreasing KL divergence (first column in Figure 3), likely because the

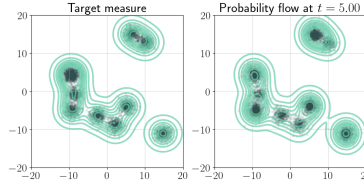


Figure 1: Qualitative comparison between the target mixture of 10 Gaussians in dimension 60 and the probability flow solution of SCVM-NODE at $t = 5$. Samples are projected onto the first two PCA components and kernel density estimation is used to generate the contours.

optimization at each JKO step has yet to reach the minimum even though we use 2000 gradient updates for each step.

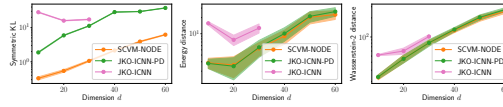


Figure 2: Quantitative comparison for the mixture of Gaussians experiment across dimension d at $t = 5$.

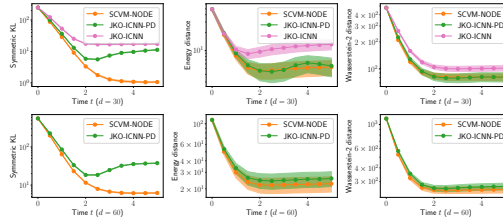


Figure 3: Quantitative comparison for the mixture of Gaussians experiment for varying t in dimension 30 (top row) and 60 (bottom row).

To illustrate the computational bottleneck of JKO-based methods, in Figure 4, we plot the run time (in seconds) of each JKO step for the JKO-ICNN and JKO-ICNN-PD for dimension 20. For both methods, the running time for each JKO step increases linearly because samples (and for JKO-ICNN also log det terms) need to be pushed through a growing chain of ICNNs; as a result, the total running time scales quadratically with the number of JKO steps. The memory consumption scales linearly with the number of JKO steps as well which can become prohibitive. For $d = 20$, training SCVM-NODE took only 6.78 minutes, while JKO-ICNN and JKO-ICNN-PD with 40 JKO steps took 29.28 and 137.66 minutes respectively. JKO methods also take about 10x as long evaluation time as SCVM-NODE in dimension 20 (and more in higher dimensions) due to density access which requires solving an optimization problem for each JKO step. On top of the computational advantage and the better results, our method also does not have temporal discretization: after being trained, the flow can be accessed at any time t (Figure 14).

4.2 ORNSTEIN-UHLENBECK PROCESS

To compare the accuracy of the obtained solution at all time t , we consider the Ornstein-Uhlenbeck (OU) process following the same experimental setup as in Mokrov et al. (2021); Fan et al. (2021). The OU process is the Wasserstein gradient flow of the KL divergence with respect to a Gaussian $\mu^* = \mathcal{N}(\beta, \Gamma^{-1})$ where $\beta \in \mathbf{R}^d$ and Γ is a $d \times d$ positive-definite matrix. When the initial distribution is $\mu_0^* = \mathcal{N}(0, I_d)$, the gradient flow at time t is known to be a Gaussian distribution $G(t)$ with mean $(I_d - e^{-t\Gamma})\beta$ and covariance $\Gamma^{-1}(I_d - e^{-2t\Gamma}) + e^{-2t\Gamma}$. We set the total time $T = 2$. We consider both SCVM-TIPF and SCVM-NODE.

In Figure 5, for each method, we compute the symmetric KL and the symmetric f -divergence between the recovered measure at time t and $G(t)$ as functions of t in dimension $d = 5$ and $d = 10$. We

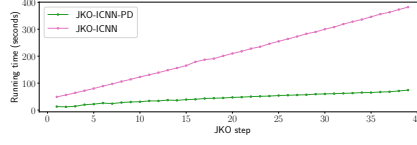


Figure 4: Running time for each JKO step in dimension 20 of a particular run for the mixture of Gaussians experiment.

found that JKO methods result in much higher errors for small t compared to both SCVM-TIPF and SCVM-NODE: this is expected because the dependency of $G(t)$ on t is exponential, so convergence to μ^* is faster in the beginning, yet a constant step size is used for JKO methods. In Figure 6, we compute the same metrics at final time $t = T$ as functions of dimension d for $d = 2, 3, \dots, 10$ (top row) and $d = 10, 20, \dots, 60$ (bottom row). We see that SCVM-TIPF gives the best results in low dimensions; however, scaling it to $d \geq 10$ is difficult as many coupling layers are needed. In high dimensions, both JKO-ICNN methods achieve good results. We suspect this is because the network architecture for ICNN has convex quadratic skip connections, the gradients of which are linear maps so ICNN methods excel at learning linear maps which are sufficient for recovering the OU process. Indeed, if we replace the convex quadratic skip connections with linear connections—this is closer to the original ICNN (Amos et al., 2017)—then the performance of JKO-ICNN and JKO-ICNN-PD drops drastically and results in numbers worse than those of SCVM-NODE (Figure 15).

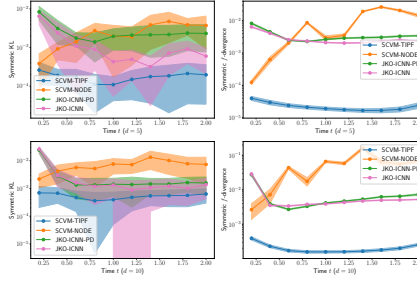


Figure 5: Symmetric KL and f -divergence for the OU process experiment as functions of t in dimension 5 (top row) and 10 (bottom row).

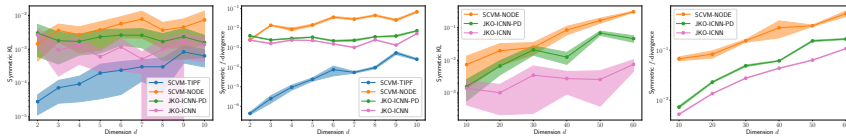


Figure 6: Symmetric KL and f -divergence at $t = T$ for the OU process experiment as functions of dimension. Top: $d = 2, 3, \dots, 10$. Bottom: $d = 10, 20, \dots, 60$.

4.3 POROUS MEDIUM EQUATION

Following Fan et al. (2021), we consider the porous medium equation with only diffusion: $\partial_t p_t = \Delta p_t^m$ with $m > 1$. It is the Wasserstein gradient flow of $\mathcal{F}(\mu) = \int \frac{1}{m-1} p(x)^m dx$ where p is the density of μ . The corresponding Wasserstein gradient is $\nabla_{W_2} \mathcal{F}(\mu)(x) = mp^{m-2}(x)$. This flow has as closed-form solution given by the Barenblatt profile Vázquez (2007) when initialized accordingly:

$$p_t^*(x) = (t + t_0)^{-\alpha} \left(C - \beta \|x\|^2 (t + t_0)^{-\frac{2\alpha}{d}} \right)_+^{\frac{1}{m-1}}, \quad (11)$$

where $t_0 > 0$ is the starting time, $\alpha = \frac{m}{d(m-1)+2}$, $\beta = \frac{(m-1)\alpha}{2dm}$, and $C > 0$ is a free constant. We do not consider SCVM-NODE here because the integration-by-part trick (Proposition 3.1) does not apply. Similar to Fan et al. (2021), we choose $m = 2$ and total time $T = 0.025$. The initial

measure follows a Barenblatt distribution supported in $[-0.25, 0.25]^d$ (C is chosen accordingly) with $t_0 = 10^{-3}$. We use Metropolis-Hastings to sample from μ_0 .

We show the efficiency of SCVM-TIPF compared to JKO-ICNN in dimension $d = 1, 2, \dots, 6$. We exclude JKO-ICNN-PD since it produces significantly worse results on this application. We visualize the density p_t of the recovered flow from SCVM-TIPF and JKO-ICNN in Figure 7 in dimension 1 compared to p_t^* . Both methods approximate p_t^* well with SCVM-TIPF more precise at the beginning of the flow; this is consistent with the observation in Figure 5 where JKO methods result in bigger errors for small t .

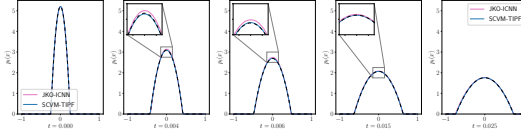


Figure 7: Visualization of the densities of p_t^* and p_t for the porous medium equation in dimension 1 at varying time steps t for SCVM-TIPF and JKO-ICNN.

In Figure 8, we plot the f -divergence, the Wasserstein-2 distance, and the total variation (TV) distance (details on the TV distance are given in Appendix B.4) between the recovered solution p_t and p_t^* for both methods at $t = 0.004$ and $t = 0.025$. We also plot in Figure 16, for dimensions 3 and 6, the evolution of the same metrics across time. Note that the values of all metrics are very low implying that the solution from either method is very accurate, with SCVM-TIPF more precise in TV distance and symmetric f -divergence, especially for $d > 3$. Like with the experiments in previous sections, JKO-ICNN is much slower to train: in dimension 6, training JKO-ICNN took 102 minutes compared to 21 minutes for SCVM-TIPF.

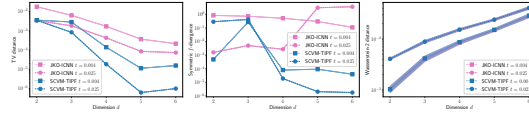


Figure 8: Total variation distance, symmetric f -divergence, and Wasserstein-2 distances across dimensions at $t = 0.004$ and $t = 0.025$ between p_t and p_t^* for solving the porous medium equation.

4.4 TIME-DEPENDENT ORNSTEIN-UHLENBECK

In this section, we qualitatively evaluate our method for solving a PDE that is not a Wasserstein gradient flow. In this case, JKO-based methods cannot be applied. Consider the OU process from Section 4.2 when the mean β and the covariance matrix Γ become time-dependent as β_t and Γ_t . The resulting PDE is a time-dependent Fokker-Planck equation of the form (4) with a velocity field

$$f_t(X, \mu_t) = \Gamma_t(\beta_t - X) - D\nabla \log p_t(X). \quad (12)$$

In this configuration, when the initial measure p_0 is Gaussian, the solution μ_t can again be shown to be Gaussian with mean and covariance following an ODE. More details are given in Appendix C.1. Following Boffi & Vanden-Eijnden (2022), we consider, in dimension 2 and 3, time-dependent attraction towards a harmonic mean $\beta_t = a(\sin(\pi\omega t), \cos(\pi\omega t))$, augmented to $\beta_t = a(\sin(\pi\omega t), \cos(\pi\omega t), t)$ in dimension 3.

We apply both SCVM-TIPF and SCVM-NODE to this problem and compare our results with those of SDE-EM, the particle-based Euler-Maruyama discretization of the stochastic differential equation associated with the Fokker-Planck equation. We did not compare against Boffi & Vanden-Eijnden (2022) because their method uses only 50 particles. To compute metrics for SDE-EM, we use kernel density estimation on the evolving particles. Similar to what has been observed for the static OU process, SCVM-TIPF outperforms SCVM-NODE in these low dimensions. SCVM-TIPF also obtains better results than SDE-EM. Visual simulations of the evolution of a few sampled particles are given Figure 17 and Figure 18.

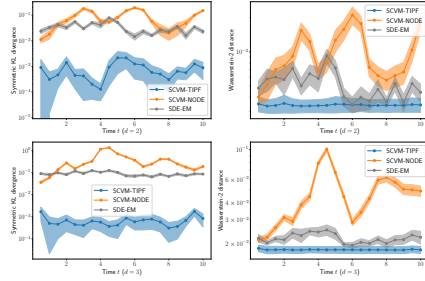


Figure 9: Symmetric KL divergence and Wasserstein-2 distances across time for $d = 2, 3$ between the recovered flows and the ground truth for the time-dependent OU process.

4.5 ADDITIONAL QUALITATIVE EXPERIMENTS

To demonstrate the flexibility of our method, we apply our algorithm to model more general mass-conserving dynamics than the ones considered in the previous sections. Animated GIFs of these dynamics can be found at [this link](#).

Flock of birds. We first propose to model the dynamics of a flock of birds by augmenting the time-dependent Fokker-Planck equation (12) with an interaction term:

$$f_t(X, \mu_t) = \Gamma_t(\beta_t - X) + \alpha_t(X - \mathbf{E}[\mu_t]) - D\nabla \log p_t(X).$$

Since f_t needs to access $\mathbf{E}[\mu_t]$, the resulting PDE is not a Fokker-Planck equation (4) but can be solved with our method by estimating $\mathbf{E}[\mu_t]$ using Monte Carlo on samples from μ_t . We use a similar setup as in Section 4.4, except we now use an “infinity sign” attraction $\beta_t = a(\cos(2\pi\omega t), 0.5 \sin(2\pi\omega t))$ along with a sinusoidal $\alpha_t = 2 \sin(\pi\omega t)$. Depending on the sign of α_t , particles are periodically attracted towards or repulsed from their mean. Both SCVM-TIPF and SCVM-NODE produce similar visual results as shown in Figure 10 and Figure 20.

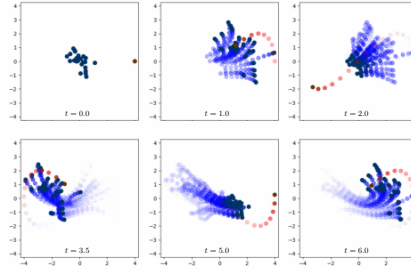


Figure 10: Flow at a few sampled particles of SCVM-TIPF which simulates a flock of birds. See Figure 19 for visualization with more time steps.

Flow splashing against obstacles. We now model the phenomenon of a 2-dimensional flow splashing against obstacles using a Fokker-Planck equation (4) where b_t encodes the configuration of three obstacles that repel the flow (See Appendix C.3 for details). We solve this PDE using SCVM-NODE for $T = 5$ and visualize the recovered flow in (11). When solving the same PDE using SDE-EM, the flow incorrectly crosses the bottom right obstacle due to a finite time step size (Figure 22) whereas our method has no such issue and results in continuous sample paths (Figure 21).

Smooth interpolation of measures. We formulate the problem of smoothly interpolating a list of measures as a time-dependent Fokker-Planck equation and use it to interpolate MNIST digits 1, 2, and 3, starting from a Gaussian (Figure 12). We use a mixture of small-variance Gaussians to represent each digit given as an image. See Appendix C.4 for more details.

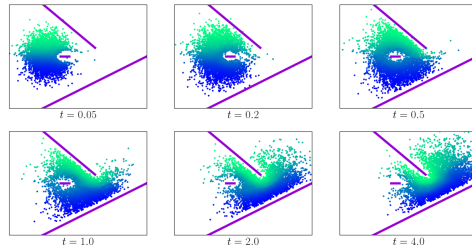


Figure 11: A flow splashing against three obstacles (in purple). Particles are colored based on the initial y coordinates.

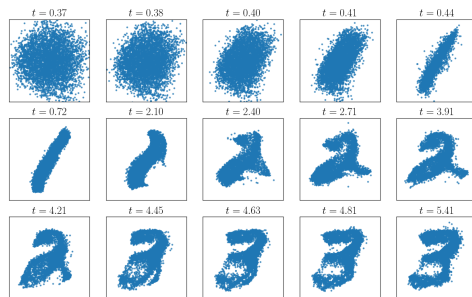


Figure 12: Flow at selected time steps that interpolate MNIST digits 1, 2, 3 starting from a Gaussian, computed using SCVM-NODE.

5 CONCLUSION

By extending the concept of self-consistency from Shen et al. (2022), we present an iterative optimization method for solving a wide class of mass-conserving PDEs without temporal or spatial discretization. Our method achieves strong quantitative results in computing Wasserstein gradient flows compared to recent JKO-based methods while requiring far less computation time.

Below we highlight three directions for future work. First, as discussed, the two ways to parameterize a probability flow, TIPF and NODE, both have their specific limitations. Finding a new parameterization that combines the advantages of both TIPF and NODE is an important next step. We also hope to extend our approach to incorporate more complicated boundary conditions. Finally, from a theoretical perspective, it would be interesting to explore the convergence properties of the proposed iterative procedure.

REFERENCES

- David Alvarez-Melis, Yair Schiff, and Youssef Mroueh. Optimizing functionals on the space of probabilities with input convex neural networks. *arXiv preprint arXiv:2106.00774*, 2021.
- Luigi Ambrosio, Nicola Gigli, and Giuseppe Savaré. *Gradient flows: in metric spaces and in the space of probability measures*. Springer Science & Business Media, 2005.
- Brandon Amos, Lei Xu, and J Zico Kolter. Input convex neural networks. In *International Conference on Machine Learning*, pp. 146–155. PMLR, 2017.
- Jonathan T Barron. Continuously differentiable exponential linear units. *arXiv preprint arXiv:1704.07483*, 2017.
- Marin Biloš, Johanna Sommer, Syama Sundar Rangapuram, Tim Januschowski, and Stephan Günnemann. Neural flows: Efficient alternative to neural odes. *Advances in Neural Information Processing Systems*, 34:21325–21337, 2021.

- Mathieu Blondel, Quentin Berthet, Marco Cuturi, Roy Frostig, Stephan Hoyer, Felipe Llinares-López, Fabian Pedregosa, and Jean-Philippe Vert. Efficient and modular implicit differentiation. *arXiv preprint arXiv:2105.15183*, 2021.
- Nicholas M Boffi and Eric Vanden-Eijnden. Probability flow solution of the fokker-planck equation. *arXiv preprint arXiv:2206.04642*, 2022.
- Nicolas Bonneel, Michiel Van De Panne, Sylvain Paris, and Wolfgang Heidrich. Displacement interpolation using lagrangian mass transport. In *Proceedings of the 2011 SIGGRAPH Asia conference*, pp. 1–12, 2011.
- James Bradbury, Roy Frostig, Peter Hawkins, Matthew James Johnson, Chris Leary, Dougal Maclaurin, George Necula, Adam Paszke, Jake VanderPlas, Skye Wanderman-Milne, and Qiao Zhang. JAX: composable transformations of Python+NumPy programs, 2018. URL <http://github.com/google/jax>.
- Martin Burger, José A Carrillo, and Marie-Therese Wolfram. A mixed finite element method for nonlinear diffusion equations. *Kinetic & Related Models*, 3(1):59, 2010.
- José A Carrillo, Alina Chertock, and Yanghong Huang. A finite-volume method for nonlinear non-local equations with a gradient flow structure. *Communications in Computational Physics*, 17(1): 233–258, 2015.
- Ricky TQ Chen, Yulia Rubanova, Jesse Bettencourt, and David K Duvenaud. Neural ordinary differential equations. *Advances in neural information processing systems*, 31, 2018.
- Dan Crisan and Terry Lyons. A particle approximation of the solution of the kushner–stratonovitch equation. *Probability Theory and Related Fields*, 115(4):549–578, 1999.
- Lauro Langosco di Langosco, Vincent Fortuin, and Heiko Strathmann. Neural variational gradient descent. *arXiv preprint arXiv:2107.10731*, 2021.
- Laurent Dinh, Jascha Sohl-Dickstein, and Samy Bengio. Density estimation using real nvp. *arXiv preprint arXiv:1605.08803*, 2016.
- Jiaojiao Fan, Amirhossein Taghvaei, and Yongxin Chen. Variational wasserstein gradient flow. *arXiv preprint arXiv:2112.02424*, 2021.
- Jonathan Heek, Anselm Levskaya, Avital Oliver, Marvin Ritter, Bertrand Rondepierre, Andreas Steiner, and Marc van Zee. Flax: A neural network library and ecosystem for JAX, 2020. URL <http://github.com/google/flax>.
- Desmond J Higham. An algorithmic introduction to numerical simulation of stochastic differential equations. *SIAM review*, 43(3):525–546, 2001.
- Aapo Hyvärinen and Peter Dayan. Estimation of non-normalized statistical models by score matching. *Journal of Machine Learning Research*, 6(4), 2005.
- Richard Jordan, David Kinderlehrer, and Felix Otto. The variational formulation of the fokker–planck equation. *SIAM journal on mathematical analysis*, 29(1):1–17, 1998.
- George Em Karniadakis, Ioannis G Kevrekidis, Lu Lu, Paris Perdikaris, Sifan Wang, and Liu Yang. Physics-informed machine learning. *Nature Reviews Physics*, 3(6):422–440, 2021.
- Diederik P Kingma and Jimmy Ba. Adam: A method for stochastic optimization. *arXiv preprint arXiv:1412.6980*, 2014.
- Yaron Lipman, Ricky TQ Chen, Heli Ben-Hamu, Maximilian Nickel, and Matt Le. Flow matching for generative modeling. *arXiv preprint arXiv:2210.02747*, 2022.
- Xingchao Liu, Chengyue Gong, and Qiang Liu. Flow straight and fast: Learning to generate and transfer data with rectified flow. *arXiv preprint arXiv:2209.03003*, 2022.

- Petr Mokrov, Alexander Korotin, Lingxiao Li, Aude Genevay, Justin M Solomon, and Evgeny Burnaev. Large-scale wasserstein gradient flows. *Advances in Neural Information Processing Systems*, 34:15243–15256, 2021.
- Gabriel Peyré. Entropic approximation of wasserstein gradient flows. *SIAM Journal on Imaging Sciences*, 8(4):2323–2351, 2015.
- Maziar Raissi, Paris Perdikaris, and George E Karniadakis. Physics-informed neural networks: A deep learning framework for solving forward and inverse problems involving nonlinear partial differential equations. *Journal of Computational physics*, 378:686–707, 2019.
- Hannes Risken and Hannes Risken. *Fokker-planck equation*. Springer, 1996.
- Filippo Santambrogio. Optimal transport for applied mathematicians. *Birkäuser, NY*, 55(58-63):94, 2015.
- Zebang Shen, Zhenfu Wang, Satyen Kale, Alejandro Ribeiro, Aim Karbasi, and Hamed Hassani. Self-consistency of the fokker-planck equation. *arXiv preprint arXiv:2206.00860*, 2022.
- Gábor J Székely and Maria L Rizzo. Energy statistics: A class of statistics based on distances. *Journal of statistical planning and inference*, 143(8):1249–1272, 2013.
- Juan Luis Vázquez. *The porous medium equation: mathematical theory*. Oxford University Press on Demand, 2007.
- Michael Westdickenberg and Jon Wilkening. Variational particle schemes for the porous medium equation and for the system of isentropic euler equations. *ESAIM: Mathematical Modelling and Numerical Analysis*, 44(1):133–166, 2010.

A INTEGRATION-BY-PARTS TRICK

This is a common trick used in score-matching literature (Hyvärinen & Dayan, 2005).

Proof of Proposition 3.1. Fix $t > 0$. The form of f_t in (4) is

$$f_t(x; \mu_t) = b_t(x) - D_t(x) \nabla \log p_t(x).$$

Hence

$$\mathbf{E}_{X \sim \mu_t^{\theta'}} \left[v_t^\theta(X)^\top f_t(X; \mu_t^{\theta'}) \right] = \mathbf{E}_{X \sim \mu_t^{\theta'}} \left[v_t^\theta(X)^\top b_t(X) \right] - \mathbf{E}_{X \sim \mu_t^{\theta'}} \left[v_t^\theta(X)^\top D_t(x) \nabla \log p_t^{\theta'}(x) \right].$$

The second term can be written as

$$\begin{aligned} \mathbf{E}_{X \sim \mu_t^{\theta'}} \left[v_t^\theta(X)^\top D_t(x) \nabla \log p_t(x) \right] &= \int v_t^\theta(X)^\top D_t(x) \nabla \log p_t^{\theta'}(x) \, d p_t^{\theta'}(x) \\ &= \int v_t^\theta(X)^\top D_t(x) \nabla p_t^{\theta'}(x) / p_t^{\theta'}(x) \cdot p_t^{\theta'}(x) \, dx \\ &= \int v_t^\theta(X)^\top D_t(x) \nabla p_t^{\theta'}(x) \, dx \\ &= - \int \nabla \cdot (D_t(x)^\top v_t^\theta(X)) p_t^{\theta'}(x) \, dx \\ &= - \mathbf{E}_{X \sim \mu_t^{\theta'}} \left[\nabla \cdot (D_t(x)^\top v_t^\theta(X)) \right], \end{aligned}$$

where we use integration-by-parts to get the second last equation and the assumption that v_t^θ , D_t are bounded and $p_t^{\theta'}(x) \rightarrow 0$ as $\|x\| \rightarrow \infty$. \square

B IMPLEMENTATION DETAILS

B.1 NETWORK ARCHITECTURES FOR SCVM.

For TIFP, our implementation follows Dinh et al. (2016). Each coupled layer uses 3-layer fully-connected networks with layer size 64, 128, 128 for both scale and translation prediction. We use twice as many coupling layers as the dimension of the problem while each coupling layer updates one coordinate; we found using fewer layers with random masking gives much worse results.

For NODE, we use a 4-layer fully-connected network for modeling the velocity field with layer size 128.

We use CELU activation (Barron, 2017) which is continuously differentiable for all layers for both TIFP and NODE.

We also add a sinusoidal embedding for the time input t plus two fully-connected layers of size 64 before concatenating it with the spatial input. The numerical integration for NODE is done using the built-in `odeint` from JAX with a relative and absolute tolerance of 10^{-3} ; we did not find considerable improvement when using a lower tolerance.

We always use the integration-by-parts trick for SCVM-NODE whenever possible. Since TIFP has tractable log density, we do not use such a trick and optimize (9) directly for SCVM-TIFP which we found to produce better results.

B.2 HYPERPARAMETERS.

Unless mentioned otherwise, we choose the following hyperparameters for Algorithm 1. We set $N_{\text{train}} = 10^5$, $B = 1000$, $L = 20$. We use $N_{\text{inner}} = 1$ in all experiments: while using a bigger N_{inner} results in faster convergence for the outer iteration, each inner iteration takes a longer time—see a comparison in Figure 13. We use Adam (Kingma & Ba, 2014) with a cosine decay learning rate scheduler, with initial learning rate 10^{-3} , the number of decay steps same as N_{train} , and $\alpha = 0.01$ (so the final learning rate is 10^{-5}).

B.3 IMPLEMENTATION OF JKO METHODS.

We base our JAX implementation of ICNN on the codebase by the original ICNN author: <https://github.com/facebookresearch/w2ot>. Compared to the original ICNN implementation by Amos et al. (2017), we add an additional convex quadratic skip connections used by Mokrov et al. (2021), which as discussed at the end of Section 4.2, might contribute to the excellent performance of JKO methods for the OU process experiment. For ICNNs, we use hidden layer sizes 64, 128, 128, 64. The quadratic rank for the convex quadratic skip connections is set to 20. The activation layer is taken to be CELU.

To implement the method by Fan et al. (2021), we model the dual potential as a 4-layer fully-connected network with layer size 128, with CELU activation. For the gradient flow of KL divergence and generalized entropy (used in Section 4.3), we follow closely the variational formulation and the necessary change of variables detailed in Fan et al. (2021, Corollary 3.3, Corollary 3.4).

In order to compute the log density at any JKO step, following Mokrov et al. (2021), we need to solve a convex optimization to find the inverse of the gradient of an ICNN. We use the LBFGS algorithm from JAXopt (Blondel et al., 2021) to solve the optimization with tolerance 10^{-2} (except for Section 4.3 we use a tolerance of 10^{-3} to obtain finer inverses, but it takes 6x longer compared to 10^{-2}).

For each JKO step, we perform 1000 stochastic gradient descent using Adam optimizer with a learning rate of 10^{-3} , except for the mixture of Gaussians experiment, we use 2000 steps—using fewer steps will result in worse results. We have tested with the learning rate schedules used in Fan et al. (2021); Mokrov et al. (2021) and did not notice any improvement.

B.4 EVALUATION METRICS

For all our experiments, calculations of the symmetric KL divergence, the symmetric f -divergence, the energy distance, and the Wasserstein-2 distance are repeated 10 times on 1000 samples from each distribution. Our plots show both the average and the standard deviation calculated over these 10 repetitions.

For the porous medium equation (Section 4.3), the total variation distance is used in Figure 8 and Figure 16 to compare the estimated and ground-truth solutions. It is approximated by the L_1 distance between the densities calculated over 50000 samples uniformly distributed on the compact $[-1.25x_{\max}, 1.25x_{\max}]$ with $x_{\max} = C / \left(\beta(t + t_0)^{-\frac{2\alpha}{d}} \right)$ being the bound of the support of p_t^* .

C ADDITIONAL EXPERIMENTAL DETAILS

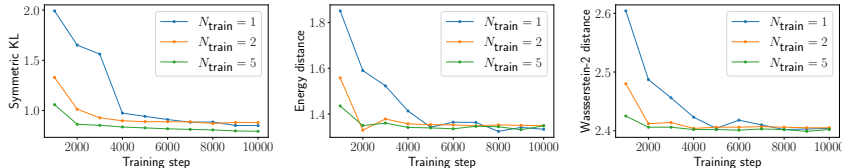


Figure 13: Metrics (after taking \log_{10}) as functions of the training step for SCVM-NODE applied to the mixture of Gaussians experiment in dimension 60. While higher values of N_{inner} converge in fewer training steps, they also take N_{inner} times longer on each step. We found different values of N_{inner} do not make a considerable difference for the same amount of training time.

C.1 TIME-DEPENDANT FOKKER-PLANCK

We give more details on the time-dependent OU process experiments presented Section 4.4. We consider a time-dependent Fokker-Planck equation of the form (4) with the velocity field

$$f_t(X, \mu_t) = \Gamma_t(X - \beta_t) - D_t \nabla \log p_t(X). \quad (13)$$

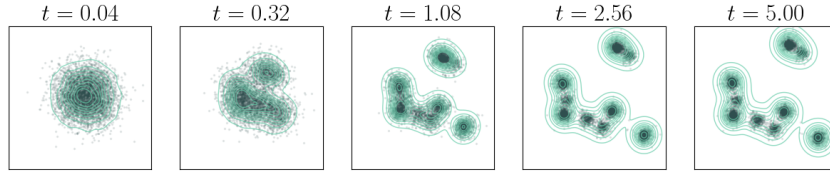


Figure 14: Probability flow at irregular time steps of our method with the same setup as in Figure 1 with SCVM-NODE. Note the gradient flow becomes almost stationary after $t = 2.5$.

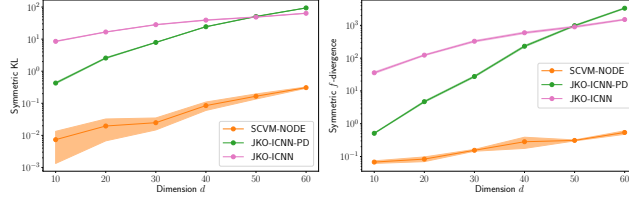


Figure 15: Symmetric KL and f -divergence at $t = T$ for the OU process experiment as functions of dimension $d = 10, 20, \dots, 60$ where the ICNN architecture used in the JKO methods is modified so that the convex quadratic skip connections are replaced with linear layers.

When the initial measure p_0 is Gaussian, the solution μ_t can again be shown to be Gaussian with mean m_t and covariance Σ_t solutions of the differential equations:

$$\begin{cases} m_t' &= -\Gamma_t(m_t - \beta_t) \\ \Sigma_t' &= -\Gamma_t \Sigma_t - \Sigma_t \Gamma_t^\top + 2D_t. \end{cases} \quad (14)$$

In practice, we experiment with constant $\Gamma_t = \text{diag}(1, 3)$ and $D_t = \sigma^2 I_d$. We also experience in dimension 3 by considering and $\Gamma_t = \text{diag}(1, 3, 1)$. We set $a = 3$, $\omega = 1$, $\sigma = \sqrt{0.25}$ and pick as initial distribution p_0 a Gaussian with mean b_0 and covariance $\sigma^2 I_d$. We set the total time to $T = 10$.

We plot in Figure 17, for dimension 2, snapshots at different time steps of particles following the flow given by our method with TIPF parametrization. We only show SCVM-TIPF because SCVM-NODE gives visually indistinguishable trajectories. We also plot in Figure 18 the evolution of particles simulated by Euler-Maruyama (EM-SDE) discretization of the Fokker-Planck equation. Corresponding animated GIFs be found at [this link](#).

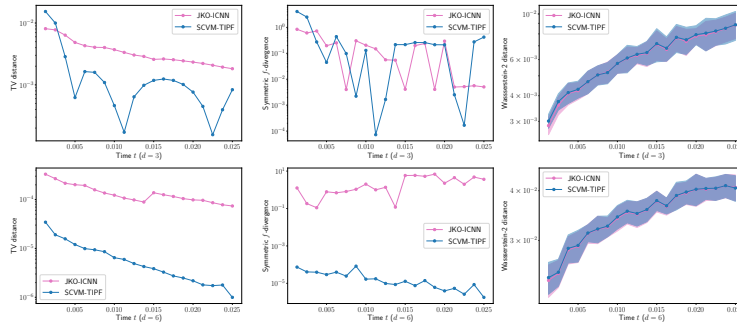


Figure 16: Metrics (TV, Symmetric f -divergence and Wasserstein-2 distance) across time for dimensions 3 and 6 between the estimated μ_t and the ground-truth μ_t^* when solving the Porous Medium Equation.

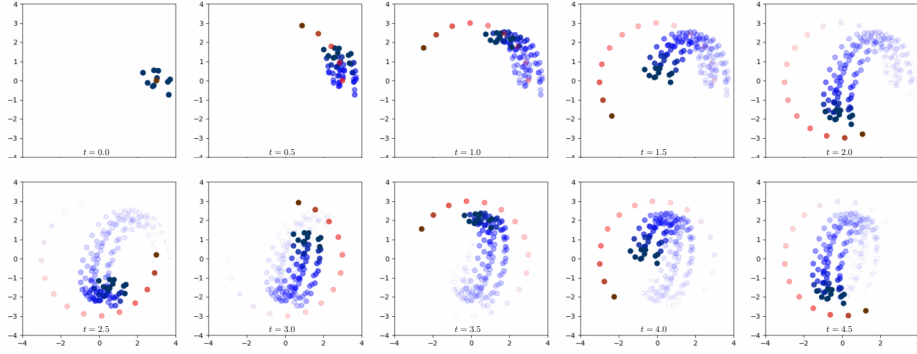


Figure 17: Evolution of particles (in blue) following the flow learned with SCVM-TIPF for the time dependant OU process (Section 4.4). In red is the moving attraction trap.

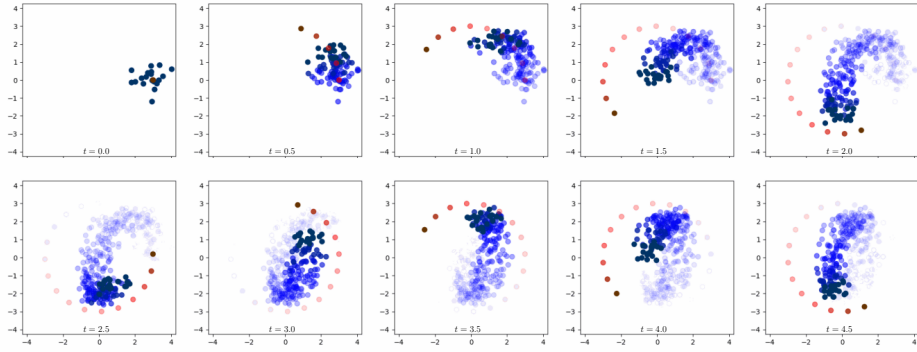


Figure 18: Evolution of particles (in blue) obtained by SDE-EM discretization for the time dependant OU process (Section 4.4). In red is the moving attraction trap.

C.2 FLOCK OF BIRDS

For this application, we use a constant $\Gamma_t = I_d$ and a constant diffusion matrix $D = \sigma^2 I_d$. We set $a = 3$, $\omega = 0.5$, and $\sigma = \sqrt{0.25}$. We pick as initial distribution p_0 a Gaussian with mean $(0, 0)$ and covariance $\sigma^2 I_d$. We set the total time to $T = 10$.

We respectively show in Figure 19 and Figure 20 simulations of particles following the flow learned with SCVM-TIPF and SCVM-NODE. Corresponding animated GIFs be found at [this link](#).

C.3 FLOW SPLASHING AGAINST OBSTACLES

We use the following formulation for modeling the flow. Each obstacle is modeled as a line segment. The endpoints of the three obstacles are:

$$((0, 3), (3, 0.5)), ((1, 0), (1.5, 0)), ((-2, -4), (6, 0)).$$

We model the dynamics as a Fokker-Planck equation where f_t of the form (4) is defined as

$$b_t(x) = (q_{\text{sink}} - x) + 20 \sum_{i=1}^3 \frac{x - \pi_{O_i}(x)}{\|x - \pi_{O_i}(x)\|} p_{\mathcal{N}(0,0.04)}(\|x - \pi_{O_i}(x)\|),$$

$$D_t(x) = I_2,$$

where $q_{\text{sink}} = (4, 0)$, and $\pi_{O_i}(x)$ is the projection of x onto obstacle i represented as a line segment, and $p_{\mathcal{N}(0,0.04)}$ is the density of an 1-dimensional Gaussian with variance 0.04.

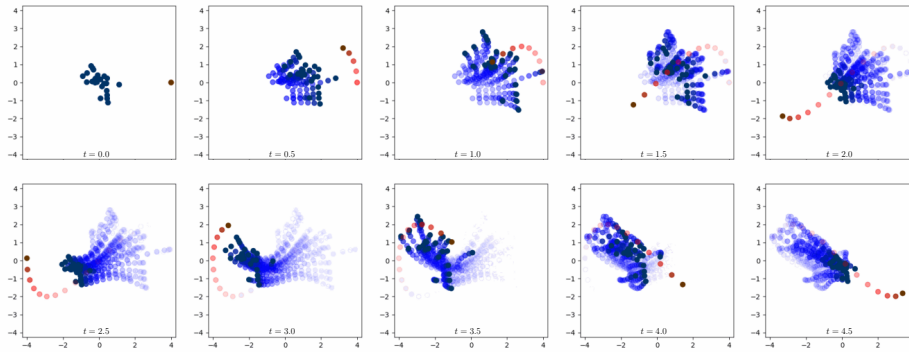


Figure 19: Evolution of particles following the flow trained with TIPF parametrization on the flock of birds PDE (Section 4.5). In red the moving attraction mean.

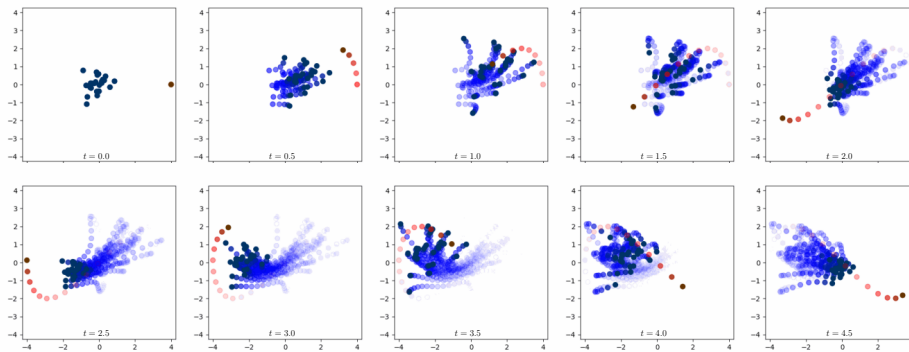


Figure 20: Evolution of particles following the flow trained with NODE parametrization on the flock of birds PDE (Section 4.5). In red the moving attraction mean.

The initial distribution is chosen to be $\mathcal{N}(0, 0.25I_2)$. We train SCVM-NODE for 10^4 with an initial learning rate of 10^{-4} . Training takes 5.4 minutes. The time step size for SDE-EM used to produce Figure 22 is 0.005.

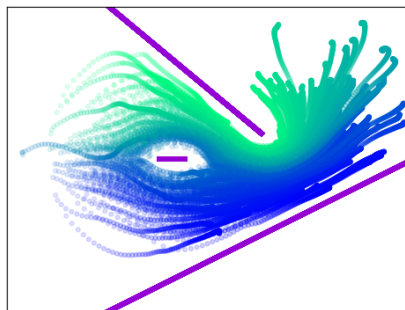


Figure 21: Trajectory of 200 random particles across time for the same setup as in Figure 11.

C.4 SMOOTH INTERPOLATION OF MEASURES

Suppose we are to interpolate M measures ν_1, \dots, ν_M with densities q_1, \dots, q_M , and we want the flow to approximate ν_i at time r_i . We model the dynamics as a Fokker-Planck equation where f_t of

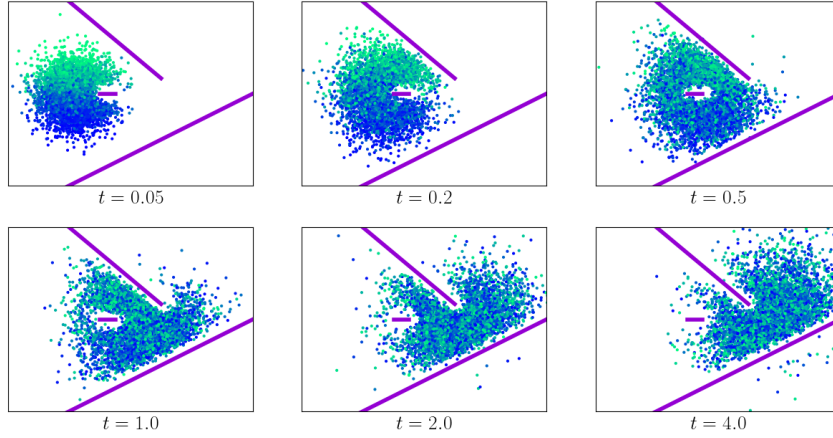


Figure 22: Same setup as in Figure 11 but with SDE-EM. We see the paths of the particles are not continuous. Moreover, the particles spill over the obstacle on the bottom right due to a finite time step size. In comparison, SCVM-NODE does not have such a problem.

the form (4) is taken to be

$$b_t(x) = \sum_{i=1}^M \phi(t - r_i) (\nabla \log q_i(x) - \nabla \log p_t(x))$$

$$D_t(x) = I_2,$$

where $\phi(t)$ is defined as the continuous bump function

$$\phi(t) = \begin{cases} 1.0 & |t| < 0.5h \\ (0.6h - |t|)/(0.1h) & |t| < 0.6h \\ 0.0 & \text{otherwise,} \end{cases}$$

for bandwidth $h = 1.0$.

We use the first three images of 1, 2, 3 from the MNIST dataset. To construct ν_i from a digit image, we use a mixture of Gaussians where we put one equally-weighted Gaussian with covariance $0.02^2 I_2$ on the pixels with values greater than 0.5 (images are first normalized to have values in $[0, 1]$). The initial distribution is $\mathcal{N}((0.5, 0.5), 0.04 I_2)$. To train SCVM-NODE, we use an initial learning rate of 10^{-4} with cosine decay for a total of 5×10^5 iterations. This takes 7 hours to train, although comparable results can be obtained after the 1-hour mark.